CONSTRAINT BASED BAYESIAN OPTIMIZATION OF BIOINK PRECURSOR: A MACHINE LEARNING FRAMEWORK

Yihao Xu

Department of Mechanical and Industrial Engineering

Northeastern University, 360 Huntington Avenue, Boston, MA 02115

xu.yiha@northeastern.edu

Rokeya Sarah

Department of Sustainable Product Design and Architecture

Keene State College, 229 Main St, Keene, NH 03435

rokeya.sarah@keene.edu

Ahasan Habib*

Department of Manufacturing and Mechanical Engineering Technology,

Rochester Institute of Technology, 70 Lomb Memorial Drive, Rochester, NY 14623, USA

mahmet@rit.edu

Yongmin Liu*

Department of Mechanical and Industrial Engineering

Department of Electrical and Computer Engineering

Northeastern University, 360 Huntington Avenue, Boston, MA 02115

y.liu@northeastern.edu

Bashir Khoda*

Department of Mechanical Engineering

The University of Maine, Ferland Engineering Education and Design Center, Orono, ME 04469

bashir.khoda@maine.edu

ABSTRACT

Current research practice for optimizing bioink involves exhaustive experimentation with multi-material composition for determining the printability, shape fidelity and biocompatibility. Predicting bioink properties can be beneficial to the research community but is a challenging task due to the non-Newtonian behavior in complex composition. Existing models such as Cross model become inadequate for predicting the viscosity for heterogeneous composition of bioinks. In this paper, we utilize a machine learning framework to accurately predict the viscosity of heterogeneous bioink compositions, aiming to enhance extrusion-based bioprinting techniques. Utilizing Bayesian optimization (BO), our strategy leverages a limited dataset to inform our model. This is a technique especially useful of the typically sparse data in this domain. Moreover, we have also developed a mask technique that can handle complex constraints, informed by domain expertise, to define the feasible parameter space for the components of the bioink and their interactions. Our proposed method is focused on predicting the intrinsic factor (e.g., viscosity) of the bioink precursor which is tied to the extrinsic property (e.g., cell viability) through the mask function. Through the optimization of the hyperparameter, we strike a balance between exploration of new possibilities and exploitation of known data, a balance crucial for refining our acquisition function. This function then guides the selection of subsequent sampling points within the defined viable space and the process continues until convergence is achieved, indicating that the model has sufficiently explored the parameter space and identified the optimal or near-optimal solutions. Employing this AI-guided BO framework, we have developed, tested, and validated a surrogate model for determining the viscosity of heterogeneous bioink compositions. This data-driven approach significantly reduces the experimental workload required to identify bioink compositions conducive to functional tissue growth. It not only streamlines the process of finding the optimal bioink compositions from a vast array of heterogeneous options but also offers a promising avenue for accelerating advancements in tissue engineering by minimizing the need for extensive experimental trials.

Key words: 3D bioprinting, Bioink, rheology, Bayesian optimization.

1. Introduction

The ability to precisely control the deposition of materials through the adjustment of fabrication parameters makes bio-fabrication or bioprinting a promising method for regenerative medicine research in various areas, including tissue engineering, transplantation, clinical medicine, drug development, high-throughput screening, and cancer research [1-6]. As per the ASTM standard [7], most prevalent bioprinting techniques are extrusion-based techniques (e.g., microextrusion, direct writing) [8, 9], jetting-based techniques (e.g., inkjet, laser-assisted) [10, 11], and vat polymerization stereolithography (SLA) [12]. In these printing methods, cell-laden bioinks are spatially deposited and polymerized, contributing to scaffold-based bio-manufacturing. All bioprinting processes have three stages: (i) pre-processing (material preparation), (ii) processing (via deposition), and (iii) post-processing (providing transient support and facilitating cell-to-tissue growth) [13]. Depending on the specific bioprinting process and technique employed, living cells undergo various challenges and stresses at each stage of bioprinting. For example, high shear stress can arise at the nozzle tip during the extrusion process which can rupture the cell wall [14] [15]. Ink-jet bioprinting is limited to low viscosity bioink due to the smaller orifice and the dropelets can dry quickly, increasing the cell mortality rates [16]. With increases in the material viscosity, cell viability can be negatively affected due to the impact velocity, droplet volume [17]. Similarly, the absorbed energy (e.g., laser or heat) can alter the DNA or phenotype of living cells, undermining the purpose of bioprinting [18, 19]. The 3D bioprinted constructs may deviate from the desired design or shape because of their instability and tendency to collapse when subsequent layers are added. Thus, the choice and content of ink material are critical in bioprinting process for creating biological structures including living tissue and organs [20].

Bioinks and biomaterials are integral to bioprinting, where bioink is defined as the cell laden biomaterial [13, 21]. Both bioink and the precursor have spawned their own burgeoning research field dedicated to containing, maintaining, protecting, and nurturing the growth of living cells across all three stages. However, several challenges must be addressed to fully realize the potential of bioprinting. Precision with high resolution and shape fidelity is essential to mimic the shape and architecture of a specific tissue or an organ during constructs printing [22]. Supporting and protecting cells during and after printing, maintaining structural integrity and physiological environment, and promoting cell growth and functional tissue formation at high densities require bio-active bioinks that respond to spatial and temporal stimuli. Thus, combining different

biomaterials is necessary to achieve multifunctionality including biocompatibility, bio-active microenvironment, shape fidelity, and printability for successful tissue engineering applications.

Naturally derived sodium alginate is commonly used as the bioink in extrusion-based 3D bioprinting due to its biocompatibility and shear-thinning behavior, which is suitable for printability [23]. However, increasing the weight percentages and molecular weights of this material to enhance viscosity can lead to nozzle clogging, distorted prints, and reduced cell viability [3]. Achieving well-defined 3D shapes and maintaining dimensional accuracy after printing is challenging due to the low modulus of sodium alginate. The printed filament must have enough mechanical strength to support subsequent layers [1]. Creating large-scale constructs requires confirming shape accuracy, which involves minimizing dispersion and filament sagging after printing [2].

To address these challenges, researchers have explored combining sodium alginate with other materials to enhance its physical and mechanical properties. For example, carboxymethyl cellulose (CMC), a water-soluble polysaccharide and cellulose derivative, is used to adjust viscosity. CMC has a high molecular weight and can promote cell adhesion and movement through its interaction with matrix proteins [24]. Therefore, combining CMC with alginate enhances the hydrogel's properties for bioprinting application [25]. Further improvements in mechanical properties and cell adhesion have been investigated using nano-scale reinforcements like polylactic acid (PLA) nanofibers and nano-fibrillated cellulose (NFC) [24-27]. However, acidic degradation of PLA can reduce biocompatibility, and NFC coagulation can cause nozzle clogging. To address these issues, NFC-based gels are often functionalized through oxidation using 2,2,6,6-tetramethyl-1-piperidinyloxy (TEMPO) to add negatively charged carboxylate ions, known as TO-NFC [28].

Recent research has highlighted the use of composite or hybrid hydrogels as novel bioinks and precursors, leveraging their combined benefits to enhance both biological and mechanical functionality in the bioprinting process. A delicate balance between viscosity and density is suggested for composite hydrogels. Higher solid content increases density and viscosity, which can improve geometric fidelity but may restrict cell mobility, resulting in lower post-print cell growth. Additionally, extruding a highly viscous ink requires higher pressure, increasing shear

stress on the encapsulated cells, leading to reduced cell viability and higher cell death rates [29] [30-32]. Therefore, the interactions between polymeric components, such as polymerization, chain entanglement, and covalent versus hydrogen bonding, are complex but crucial factors in designing bioinks and precursors for 3D bioprinting applications. Different compositions with the same solid content can result in significantly varied biological and mechanical properties. Due to the inherent shear-thinning properties of most hydrogel materials, viscosity can vary substantially with different shear rates, reflecting bioprinting process parameters like applied pressure and nozzle diameter [33, 34]. Predicting the properties of composite hydrogel inks is complex due to the interplay between pre-processing and deposition stage during bioprinting.

Current research practice for optimizing bioinks and precursors involve exhaustive experimentation with multi-material composition to determine the printability, shape fidelity and biocompatibility. However, such a process can be time consuming, resource intensive and may yield suboptimal results due to the complex solution space. Predicting the bioink properties is challenging due to the nature of polymers and the entanglement between inter- and intra-polymeric chains [35]. In the dilute regime, the Newtonian behavior is often observed which can be predicted by using Einstein's linear prediction model [36]. For bioinks made of multiple materials, they may demonstrate non-Newtonian behavior, for which the Cross model may be used to predict the viscosity at different share rates [37]. However, the Cross model assumes a certain level of homogeneity and continuity in the material, which might not hold true for heterogeneous multi-material systems. Besides, determining the parameters such as rheological factors n and k for the complex systems can be challenging and may require extensive empirical testing. For biomanufacturing process, the prediction at different composition is functionally more attractive and necessary than predicting the viscosity of a single composition at different share rates [38, 39]. Thus, these existing models become inadequate for predicting the viscosity of heterogeneous composition of bioinks. As a result, it is critical and beneficial to develop a viscosity predicting tool for the bio-manufacturing research community to expedite the complex process of bioink development.

Machine learning (ML) algorithms are powerful tools that offers an exciting opportunity to be utilized in all three stages of bioprinting process for the development of new and innovative tissue

engineering applications, with the potential to revolutionize the field of regenerative medicine, and digital bioprinting [40, 41] [42] [43]. A machine learning methodology was employed in the pre-procesing stage of bioprinting to identify the dominant rheological properties affecting printing quality of Type I collagen [41]. The authors utilized the relatively least general generalization algorithm, an inductive logic programming (ILP) suitable for classification. High storage modulus and low yield stress were found to be the dominant factors by their machine learning analysis. Multiple regression was used to generate a simplified linear relationship for the prediction of printability. A viscosity predictive model for polymer nano-composite (PNC) was developed by coupling ML algorithms with nonequilibrium molecular dynamics (NEMD) simulations [44]. In this pure computational framework, the viscosity was calculated using NEMD under different shear rates, nano particle loadings, and temperature conditions. The generated data was used to train the ML-based QSPR models to predict the viscosity and the results are compared with physics-based Cross, Careau and Herschel−Bulkley models.

In addition, optimum printing parameters for extrusion based 3D bioprinting was determined by Hierarchical Machine Learning (HML) framework [45] and parameter optimization index (POI) [46] to achieve print fidelity of hydrogel during deposition stage. The dataset included the dimensional similarity defined as high- and low-fidelity between the original CAD designs and the resulting alginate prints by modifying print input parameters in a systematic manner. Print inputs such as ink concentration, nozzle velocity, flow rate, and nozzle diameter were parameterized by common physical variables such as viscosity, applied pressure, and shear rate. Since only alginate was considered as building block, the nonlinear complex relationship for hybrid hydrogel to define viscosity and related print inputs has yet to be elucidated. A Bayesian optimizer was developed to determine the optimal printer parameters for EnvisionTEC 3D Bioplotter with six predetermined ink compositions made of gelatin methacryloyl (GelMA) and hyaluronic acid methacrylate (HAMA) [47]. A scoring system was established via a visual assessment on filament morphology during extrusion from the needle tip and the pore architecture on layer stacking of the printed construct. The algorithm generates a probabilistic model that proposes the subsequent printing parameters. This process continues by determining the print score of the next experiment and producing a new set of print parameters until the ideal score of ‘0’ is attained, signifying that the printer has optimized the parameters of the constructs [47]. ML has

also been used during post-printing stage to maintain and analyze the quality of the printed structure by detecting the defects such as irregularities and discontinuous filament and potentially providing ways to correct the prints [48]

Various machine learning techniques have been utilized in the pursuit of material inverse design, encompassing both structural and compositional aspects [41, 49] [50]. The conventional approaches include linear regression [51], support vector regression [52], and k-nearest neighbor regression [53]. However, these methods typically necessitate a substantial dataset for training purposes and fail to account for uncertainty in predictions, which can be a crucial factor to consider in experimental measurements and applications where errors and noise are inevitable. In this regard, the Bayesian optimization (BO) method can offer significant advantages by minimizing the size of the initial dataset, requiring fewer evaluations of the function than traditional optimization methods and balancing the exploration of uncertain regions with the exploitation of potentially optimal regions. In contrast to the experimental parameter sweeping technique, BO algorithms can efficiently explore the parameter space, focusing on the regions that are likely to result in good performance while avoiding areas that are unlikely to be successful. Besides, it includes an estimate of the uncertainty associated with each prediction, which can be used to reflect the potential experimental error. The BO-based bioink optimization proposed in the literature is primarily process-driven framework where both intrinsic and extrinsic factors are considered simultaneously to determine the quality (i.e., geometry) of the printed construct. Due to the combined effect and interactions between preprocessing and deposition parameters, the investigation can be trapped and biased towards a localized parameter space with limited experimental data. As a result, using such a framework makes it difficult to differentiate the process physics related to intrinsic and extrinsic factors.

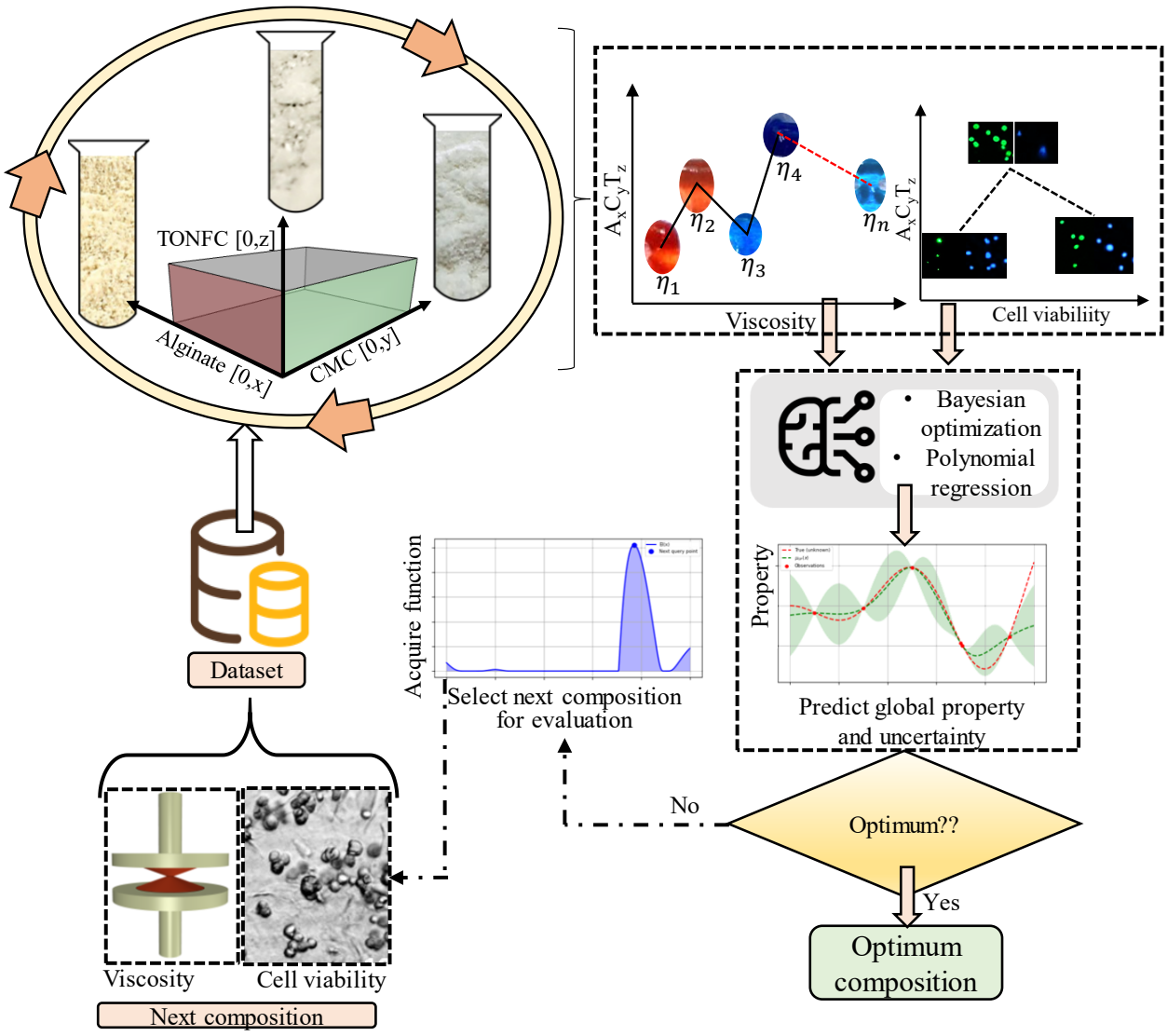

Figure 1. Schematic representation of the Bayesian optimization (BO) for developing bioink for 3D bioprinting.

In this paper, we utilize a machine learning framework to predict the viscosity of heterogeneous bioink precursor compositions, aiming to enhance extrusion-based bioprinting techniques. The bioink precursor composition under investigation builds upon our prior research [54] into hybrid hydrogels, comprising alginate, carboxymethyl cellulose (CMC), and TEMPO-oxidized nanofibrillated cellulose (TO-NFC). This composition has been empirically validated for its biocompatibility—demonstrating approximately 91% cell viability—alongside its structural integrity, capable of supporting a 3D bioprinted construct with 42 layers high and 1 cm tall, and high printability, evidenced by a printability factor greater than 0.88. These results have been

thoroughly documented in our preceding publications [54] . Our approach incorporates BO, leveraging a limited dataset to inform our model, a method especially useful given the sparse data typically available in this domain. We construct a mask function, informed by domain expertise, to define the feasible parameter space for the components of the bioink and their interactions. Through the optimization of the hyperparameter κ, we strike a balance between exploration of new possibilities and exploitation of known data, a balance crucial for refining our acquisition function (Supplementary Figure S1). This function then guides the selection of subsequent sampling points within the defined viable space and the process continues until convergence is achieved, indicating that the model has sufficiently explored the parameter space and identified the optimal or near-optimal solutions. The proposed optimization framework is schematically shown in Figure 1. Employing this AI-guided BO framework, we have developed, tested, and validated a predictive model for determining the viscosity of heterogeneous bioink compositions. The framework is able to differentiate the contributions of individual components of the heterogeneous ink material by predicting the viscosity of the same solid content with different compositions. This data-driven approach significantly reduces the experimental workload required to identify bioink composition conducive to functional tissue growth. It not only streamlines the process of finding the optimal bioink composition from a vast array of heterogeneous options but also provides a promising path to accelerate advancements in tissue engineering by reducing the necessity for extensive experimental trials.

2. Materials and Methods

2.1 Preparation of Heterogeneous Bioink Precursors

Dry TEMPO nano-fibrillated cellulose (TO-NFC) $[(C_6H_{10}O_5)_x(C_6H_9O_4CO_2Na)_y]$ with a carboxylate content ranging from 0.2 to 2 mmol/g solids was sourced from the Process Development Center (PDC) at the University of Maine. Suspensions of TO-NFC at concentrations of 0.5% and 1.0% (w/v) were prepared by stirring at 600 rpm for 24 hours at ambient temperature using a magnetic stand-up stirrer. Various concentrations of medium-viscosity Alginate (1, 2, 3, and 4%, w/v) and Carboxymethyl Cellulose (CMC) (1, 2, 3, 4, 5, and 6%, w/v) were added to these suspensions. Both Alginate (viscosity ≥2000 cps of 2% in water) and CMC (pH: 6.80) were procured from Sigma-Aldrich in St. Louis, MO, USA. The additions were made using the magnetic

stand-up stirrer to ensure homogeneous mixing of the components. The addition of CMC and TO-NFC increased the overall viscosity of the material, helping to achieve better printability and shape fidelity. A schematic diagram of preparation process of hydrogels is shown in Figure 2. The letters 'A', 'C', and 'T' denote Sodium Alginate, Carboxymethyl Cellulose, and Tempo-Mediated Nano Fibrillated Cellulose, respectively. The numerical subscripts attached to these letters indicate the weight percentage of each respective component that is incorporated into water to create the homogeneous composition.

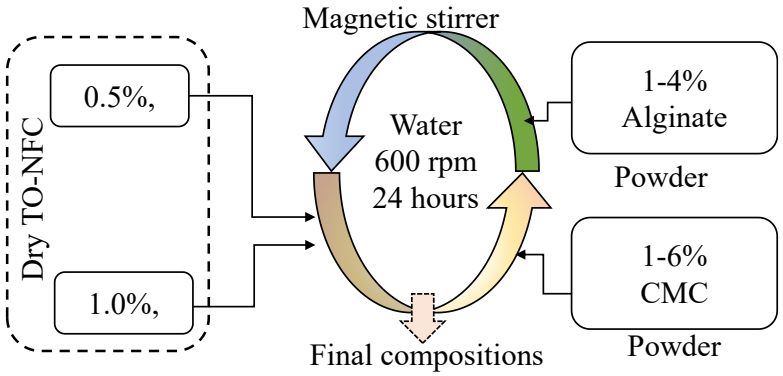

Figure 2: Schematic representation of the preparation of composition.

2.2 Determination of rheological properties

The rheological tests were conducted using a rotational rheometer (MCR 102, Anton Paar, Graz, Austria) with a parallel plate geometry (25.0 mm flat plate). The plate-to-plate gap was maintained at 1.0 mm, and all data were recorded at room temperature (25°C). The flow behavior of the compositions was considered during the rheological tests. For the proposed ML framework, a steady rate sweep test was conducted to determine the viscosities for all compositions at a shear rate of 1 s^{-1}, which can be assumed to represent the material at rest (preprocessing stage). The typical shear rate experienced by the ink at the nozzle tip during the extrusion-based bioprinting process ranges from 100 to 1,000 s^{-1}, which resemble the processing or deposition stage of bioprinting. This range depends on both the material properties (e.g., solid content, degree of polymerization, polymer chain morphology) and printing parameters (e.g., applied pressure, nozzle size, and geometry). Although the proposed data-driven BO framework is not restricted to the specific shear rate, to reduce uncertainty and variability, it has been decided to consider the intrinsic properties of the compositions at rest by isolating the effects of print parameters. Graphs

were generated using OriginPro 2022b (Originlab, Northampton, MA, USA), unless otherwise stated.

2.3 Cell culture and cytotoxicity

The bioinks were formulated, and their bioactivities were assessed using passage four Porc1 airway smooth muscle cells. The Porc1 cells were cultured in high glucose DMEM/F12 medium supplemented with 10% fetal bovine serum (FBS), 100 µg/ml of penicillin and 100 µg/ml of streptomycin (Sigma-Aldrich), in a 5% CO_2 incubator at 37°C. The growth medium was changed twice a week. Following culturing in a T-75 flask (Fisher Scientific), the cells were trypsinized and subsequently centrifuged. Then, 12×10^6 cells were re-suspended in 200 µl of culture medium and combined with a 1.0 ml sterile hydrogel solution. The cells were uniformly mixed with a magnetic stirrer at a very low speed, resulting in a final cell concentration of 10×10^6 cells/ml in our bioink. The viability assessment of 2D cultured cells and bioink before printing was conducted through a live/dead assay employing Calcein Green AM and Propidium Iodide (Thermofisher, Waltham, MA).

2.4 3D bioprinting and incubation

An in-house extrusion based 3D bioprinter was used to fabricate the constructs in a BSL-2 lab environment to resemble bioprinting process and avoid contamination. Ball screw-based linear stages are used to construct the 3-axis platform, with motion control provided by a 5-axis CNC control box (Flushcut CNC, IL). G-code is generated from the vectorized tool-path using a Visual Basic-based scripting language. The prepared bioink precursor was stored in a disposal barrel reservoir (EFD, Nordson) and extruded pneumatically through a dosing nozzle (EFD, Nordson) on a stationary build plane. Constructs were printed using 250 µm nozzle diameter (ND), 4mm/s print speed (PS), 10 psi applied pressure (P), and 0.7 mm print distance (PD). Bioprinted constructs were cross-linked with 4% (w/v) $CaCl_2$, washed three times with Hanks' balanced salt solution (HBSS), and finally incubated in fresh medium with 37°C, 5% CO_2, and more than 90% humidity. The growth medium for incubated constructs was also changed twice a week. The cell viability assessment of the 3D printed constructs was conducted through a live/dead assay employing Calcein Green AM and Propidium Iodide (Thermofisher, Waltham, MA). Percentage of cell viability (number of living cells vs total cells) was determined after 10 incubation days by

the percentage of living cells with respect to the total cells observed in any specific area under the microscope. Filament and construct images were captured using the CK Olympus bright field microscope (Tokyo, Japan) and analyzed using ImageJ software. The filament with the cells was imaged using Lionheart FX automated live cell imager (Biotek, Winooski, VT, USA). The protocol is designed to capture z-stack images with a layer thickness of 50 μm. Five beacons are randomly chosen for imaging. Throughout the process of imaging various beacons, the laser power and other detector settings remain unchanged to ensure consistency. The printability (Pr) of the constructs are measured using Equation 1 and following the technique described in our earlier work [55].

$$P_r = \frac{L^2}{16A} \tag{1}$$

Here L and A are the perimeter and actual area of the printed pore.

2.5 Bayesian optimization workflow

Once the data were collected, they were used as the initial dataset to implement the BO algorithm, a machine learning tool for global optimization of black-box functions where explicit functional forms are unknown or difficult to model. It is based on the principles of Bayesian statistics and Gaussian processes. The basic idea behind BO is to use a probabilistic model to represent the relationship between the inputs and outputs of the function being optimized. The workflow of BO includes initializing the process by selecting a small number of initial points to evaluate the function and the probabilistic model is then fit to these initial observations. Next, an acquisition function is used to decide where the next observation should be made, balancing the trade-off between exploration (detect an uncertain area in the parameter space) and exploitation (detect a potential optimal area in the parameter space). The function is evaluated at the selected point and the model is updated with the new observation. BO has demonstrated remarkable effectiveness in the optimization of materials, including but not limited to shape memory alloys [56], piezoelectrics [57], and so on.

We use the scikit-optimize (skopt) package, an open-source tool, to perform the BO on the Python platform. In each iteration, the model first builds a probabilistic model of the objective function (the viscosity) using the available data. Then, the acquisition function, $u(x)$, is calculated over the entire parameter space. Here we have used the expected improvement (EI) as the acquisition function, which is defined as

$$u(x) = EI(x) = \mathbb{E}\left[\max\left(f(x) - f(x^*)\right), 0\right] \quad (2)$$

where $f(x)$ is the objective function to be maximized, and x^* is the current best point found so far.

A pseudocode representation of the proposed algorithm is shown in Figure 3. Our goal is to obtain a surrogate model that can predict and optimize the viscosity of a bioink by adjusting three parameters: A, C, and T, which represent the composition of three materials. The parameter space can be visualized as a 3D box, with $A \in [0,5]$, $C \in [0,7]$, and $T \in [0,1]$.

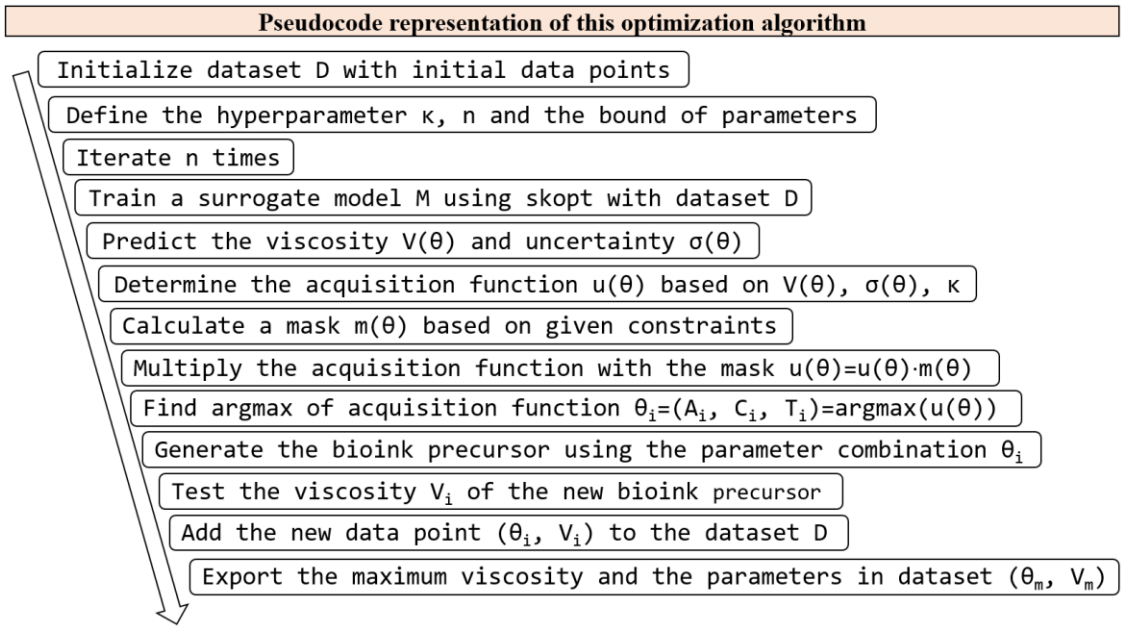

Figure 3. Pseudocode representation of the proposed optimization algorithm.

2.6 Curve fitting

To evaluate the performance of the surrogate model for viscosity prediction the of bioink precursors, a comparison was made with a conventional 4th-order polynomial curve-fitting technique. Both models were trained using varying quantities of initial data to assess their performance dependency on dataset size. The performance was determined based on mean absolute error (MAE), defined as the average of the absolute differences between the predicted values and the actual/true values in a dataset. For any fixed number of initial data points, the model yielding a lower MAE between the predicted and true viscosity values is considered superior in terms of viscosity prediction accuracy.

3 Results and discussion

3.1 Bayesian Optimization

The initial dataset comprises 47 records of heterogeneous bioink composition and corresponding viscosity data as shown in Table S1 in the Supplementary Information. Each composition was stirred for 12h-24h to ensure homogeneity. For statistical significance, a sample size of at least 3 was used for rheology data. Each record includes the composition of A, C, T (Alginate, CMC, and TO-NFC) and the viscosity value (Pa.s.). During the BO process, the three composition variables serve as inputs and the viscosity value serves as the output. The objective is to predict the material composition for the next experimental measurement, which can potentially enhance the viscosity, and establish a surrogate model to estimate the actual viscosity of any previously unseen composition, along with its error range. Overall, using BO in bioink optimization can improve efficiency and accuracy, quickly identifying optimal solutions with fewer experimental dataset. It also enables fast performance evaluation and error estimation for a given bioink composition.

The acquisition function is simpler to evaluate than the objective function, allowing us to find the next experimental point in the parameter space that maximizes the acquisition function. This process requires balancing exploration, where the model explores areas of the parameter space with higher uncertainty, against exploitation, where the model exploits areas expected to have optimized viscosity. This balance is controlled by the hyperparameter κ in skopt. A small value of κ leads the model to choose the parameter with the highest observed reward (exploitation), while a high value leads the model to choose the region with the highest variance (exploration). The effect of κ can be found in the Supplementary information, and here we set κ to 1.96 by default in the skopt model.

In our heterogeneous bioink prediction model, the parameter space consists of a 3D box without additional constraints. By adding the mask function in the proposed algorithm, complex constraints from domain experts are incorporated. As depicted in the pseudocode, in each iteration, BO is performed on the existing dataset, utilizing the calculated acquisition function. Subsequently, the parameter combination yielding the highest acquisition function value is identified. This particular combination is then utilized to create a bioink sample, which will undergo either experimental or numerical validation to determine its viscosity. Schematic representation of the proposed BO workflow is shown in Figure 4(a).

To demonstrate the effectiveness of the proposed framework, we also implemented a polynomial curve fitting function that can estimate the viscosity of a new bioink for cross-validation, since we cannot directly use the same model to verify the viscosity value of the new bioink. This function is fitted using the existing dataset and can be employed during the optimization process as a substitute for the numerical or experimental validation step. However, it is important to note that in a real optimization process, the optimization should be validated with new data points from an external source. Otherwise, there would be limited information beyond the original dataset to enhance the optimization performance. Once the viscosity value of the new bioink is obtained, this information is added as a new data point to the dataset, including the materials compositions and their corresponding viscosity value. The iterative process is then repeated until the viscosity value is optimized, achieving the desired performance for the bioink.

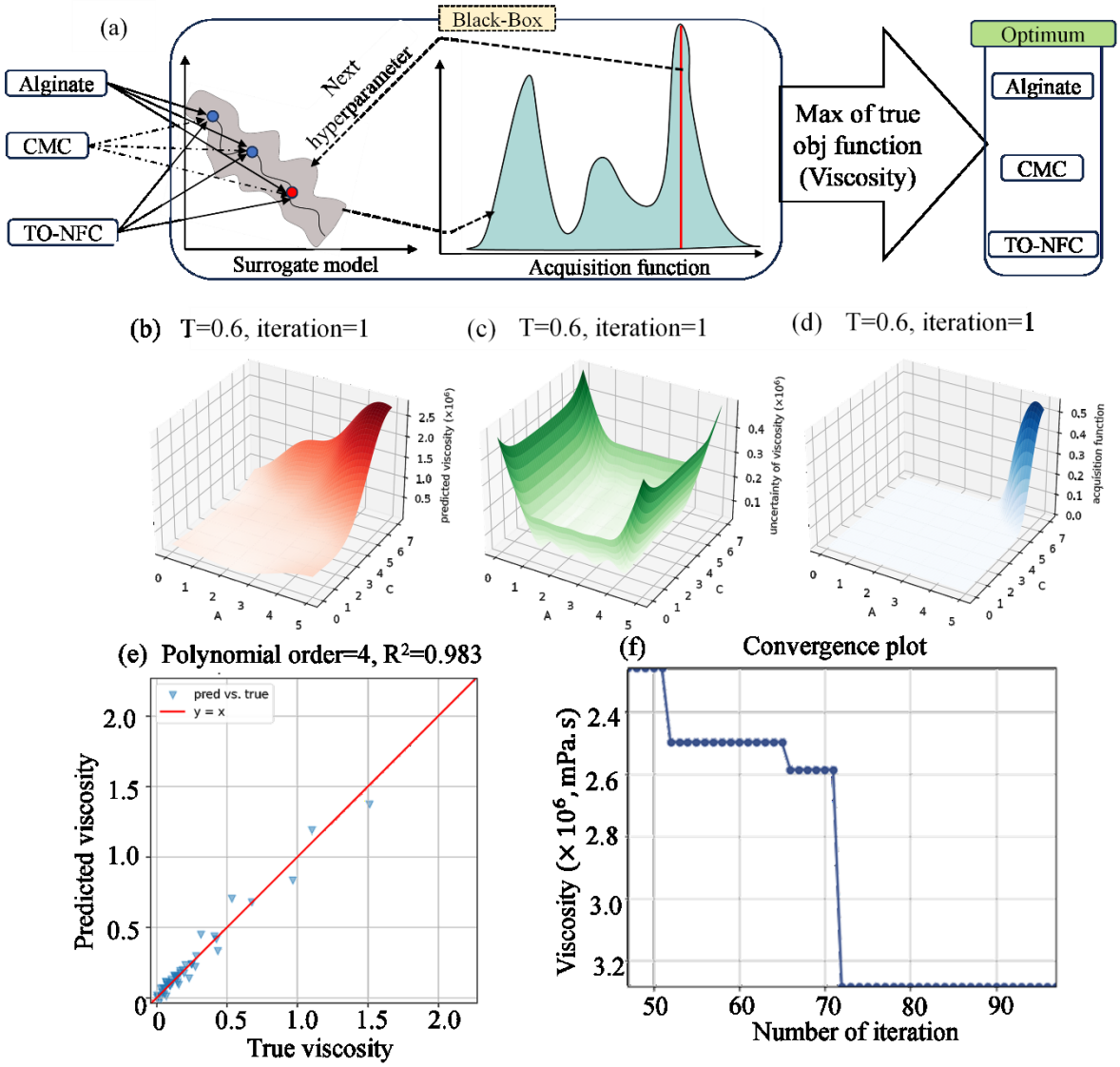

Figure 4. (a) Schematic representation of the workflow of BO. Numerical analysis of BO for viscosity prediction and optimization: (b) Predicted viscosity, (c) uncertainty of the viscosity prediction and (d) acquisition function within a slice of the parameter space after the first iteration, (e) Predicted viscosity from the polynomial fitting vs. true viscosity in the dataset, the fourth order fitting shows a R-square value to be 0.983. (f) The convergence plot of the BO after 50 iterations.

3.2 Achieving convergence

Figure 4 (b-d) presents the viscosity value, uncertainty, and acquisition function within a slice of the parameter space (A ϵ [0,5], C ϵ [0,7], and T=0.6) after the first iteration. This plot clearly demonstrates the capabilities of BO in predicting viscosity values across the entire parameter space,

along with the associated uncertainty. From the plot, it is evident that the uncertainty increases as the parameters approach the boundaries of the parameter space. This behavior is consistent with most machine learning algorithms, as they tend to perform better in interpolation rather than extrapolation tasks. To identify the next data point that has the potential for optimized viscosity, it is advantageous to select compositions where either the predicted viscosity is high, or the uncertainty is high. This concept is embodied in the acquisition function. Analyzing the plots, we observe that the viscosity increases with increasing values of A and C, and the uncertainty also becomes prominent as A and C approach their maximum values. Consequently, a peak in the acquisition function can be clearly observed at (A,C,T)=(5,7,0.6), indicating that this point should be evaluated next. To simulate a real experiment, we utilize a polynomial fitting approach with a 4th order polynomial, which achieves a high R-square value of 0.983, as depicted in Figure 4(e).

This allows us to calculate the viscosity of the composition at (A,C,T) = (5,7,0.6). The obtained viscosity value is then added to the dataset for the next iteration. It is worth emphasizing that predicting the next data point and assessing it through experimentation can be instrumental in enhancing the overall performance of the surrogate model. This is attributed to the fact that the upcoming data point may either be in proximity to a local optimum, where the values exhibit abrupt changes, or situated in an uncertain region where the accuracy of prediction may be compromised. Continuing the optimization process for 50 iterations, as illustrated in Figure 4(e), the viscosity increases from 2.2 to 3.3×10^6 mPa·s. It indicates that the viscosity has been successfully optimized to 3,300 Pa.s, highlighting the effectiveness of the BO process. The results from Figure 5 provide clear evidence of the capabilities and success of the BO process in achieving the desired viscosity optimization for the bioink.

3.3 Mask-based technique to shrink the parameter space

In many optimization space domain, the parameter space is often non-linear and unbounded. It is common for users to impose additional constraints that directly couple all parameters or define constraints on other physical metrics involving the parameters, and such constrained scenarios are also incorporated in our model. Practical optimization tasks frequently necessitate further constraints to narrow down the parameter space. For instance, without constraints, a very high solid content would likely result in excessive viscosity, which is not feasible in experiments. In such cases, constraints (e.g., A+C+T<=8%) can be valuable for restricting the parameter space to

a valid composition. Such a constraint restricts the solid content of the bioink to 8%(w/v), which has been reported as amenable for cell growth [58, 59] . Moreover, we may encounter constraints from other metrics, such as maintaining high cell viability to ensure the effectiveness of the bioink. These types of constraints may not directly impact the parameter space, making them challenging to apply directly within the optimization loop.

To address the aforementioned two types of constraints and thus increase the flexibility and generality of our optimization process, we propose a mask-based technique to apply constraints in the parameter space of the bioink optimization task. Figure 5 illustrates this approach. For the first type constraints, we can create a binary image as a mask that identifies the valid region in the parameter space. The dimensions of the mask must match the dimension of parameters, and the boundaries must match exactly. A valid composition region is indicated by a value of '1' (bright area), and an invalid composition region is indicated by a value of '0' (dark area) in the mask. The given constraints can involve single or multiple parameters, such as A+C+T<8%, 0.2<A/(C+T)<1.0, and A,C<4%, which are derived from the domain knowledge.

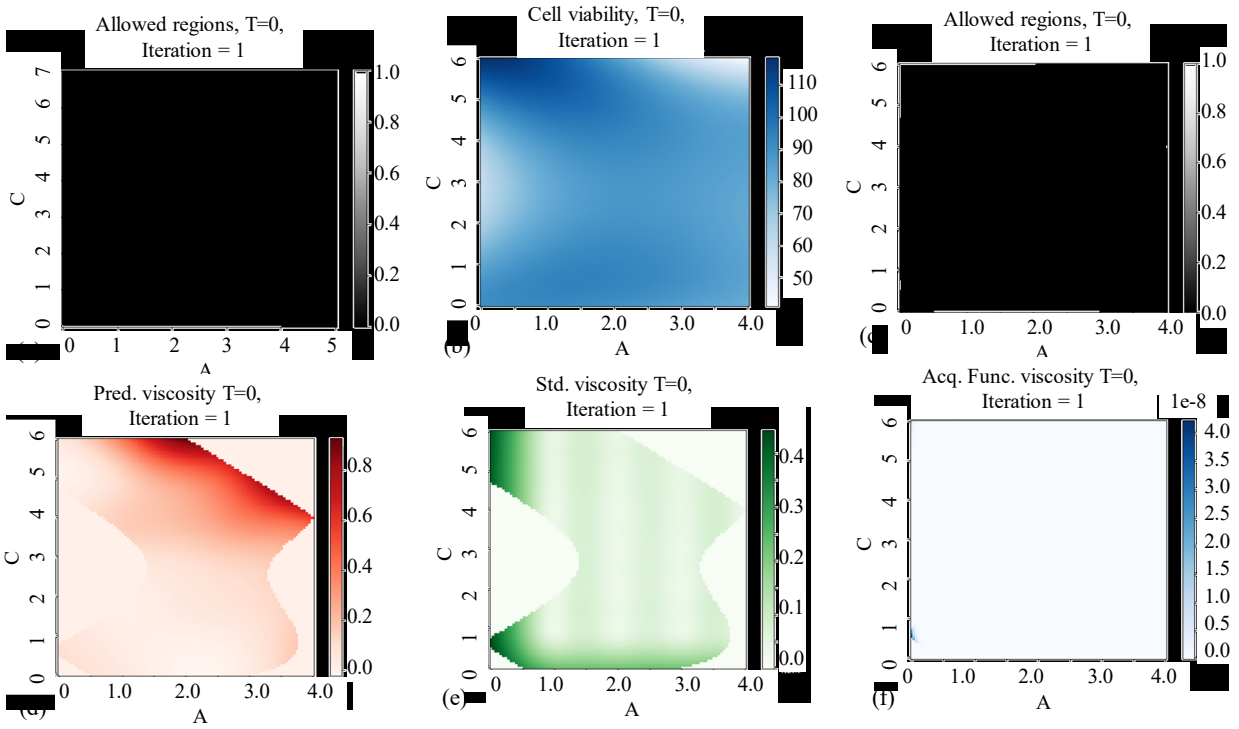

Figure 5. (a-c) Mask-based technique to shrink the parameter space into reasonable and (d-f) user-defined sub-space.

To handle the second type of constraints, we need to use a slightly different approach for creating the mask. For demonstration purposes, we assume a constraint that the cell viability should be greater than a threshold of 90%, the first step is to extract the cell viability values over the entire parameter space, which can be obtained through experimentation or interpolation from existing data. As a proof-of-concept demonstration, we use the partially available cell viability data for the composition in supplementary Table S2 and perform a polynomial fitting for the remaining composition. This experimental and simulated cell viability data is considered as the ground-truth value for demonstration (as provided in supplementary information). Figure 5b shows the cell viability values plotted for T=0. We then set the region with a value of >=90% as '1' and <90% as '0', resulting in the mask shown in Figure 5c. The boundary of the mask can be more complex, appearing as a smooth curve, which helps to address complicated constraints (Figure (d-f)). It is important to note that we can use the two kinds of masks separately or combine them to generate a mask with both types of constraints. In any case, we multiply the predicted viscosity value, standard deviation value, and acquisition function with the mask, resulting in the corresponding value in the parameter regions that meet all the constraints. Finally, we select the next point based on the parameter with the maximum acquisition function in the shrunken parameter space. Subsequent iterations are similar to the unconstrained case.

Combining the mask function with the Bayesian Optimization (BO) model offers a promising pathway for experiential machine learning, which can significantly impact the bioprinting domain in predicting the performance of bioink and precursors. In contrast to the prior literature [47] [48], our proposed method is focused on predicting the intrinsic factor (e.g., viscosity) of the bioink precursor which is tied with the extrinsic property (e.g., cell viability) through the mask function. This integration can facilitate adaptive experimentation and optimization by avoiding less relevant parameter spaces, crucial for advancing bioprinting technologies. Although, the proposed framework has been implemented on bioink precursor, the methodology can be adapted for bioink (cell-laden biomaterial) materials. The presence of cell has been reported to alter the viscosity by masking the active sites and hence the gelation mechanism [60]. However, by considering the cell as immiscible microparticles, the resultant viscosity of cell suspension can be inferred with Einstein's formula [61].

3.4 Reduction of MAE in viscosity prediction using BO technique

By implementing the BO optimization process, we obtain a surrogate model capable of predicting the viscosity of bioink without the need for experimental trials. To demonastrate the performance of the surrogate model, a comparison between BO and a 4th-order polynomial curve-fitting technique is show in Figure 6. Both models undergo training/fitting with varying quantities of initial data ranging from 10 to 58, which also assists in verifying the performance dependency on the dataset size. The plots clearly demonstrate that BO outperforms curve fitting with lower MAE of predicted data. These predictions are then compared with experimental results. It is worth noting that BO not only predicts viscosity but also provides an estimate of uncertainty. Consequently, predictions from BO are visualized as a range [$\mu-2\sigma$, $\mu+2\sigma$]. The superiority of BO in terms of prediction accuracy becomes evident, as the experimental values predominantly fall within the range predicted by BO, while curve fitting often yields predictions that deviate significantly from the experimental data. This difference is further highlighted when considering the MAE between experimental viscosity and predicted viscosityas shown in Figure 6(b). For instance, the MAE of curve fitting is nearly eight times higher than that of BO when considering a sample size of 10.

Furthermore, we observe that the prediction uncertainty and MAE, when using BO, experience a significant reduction as the size of the original dataset increases, as depicted in Figure 6(b). For instance, as the sample size increases from 10 to 30 and 50, the mean absolute prediction error (MAE) obtained through the BO technique decreases by approximately 6.7 and 8.7 times, respectively. Moreover, when comparing a sample size of 57 to 10, MAE is reduced by nearly 100 times using the BO technique. Remarkably, even with a modest set of 25 initial data points, BO consistently achieves accurate predictions well below 0.1×10^6 globally. This underscores the superior effectiveness of our proposed BO-based framework for predicting the viscosity of compositions prepared with composite hydrogels. Additionally, this technique provides users with the flexibility to initiate predictions with a predefined number of samples while accommodating a certain margin of MAE based on available resources. As illustrated in Figure 6(b), we observe fluctuations in the performance of viscosity prediction from the BO model, when the sample size is small (10-20), followed by a consistent improvement over the curve fitting model. This indicates that a modest sample size, approximately 20 in our composite hydrogel, is adequate for the BO method to surpass conventional techniques such as curve fitting.

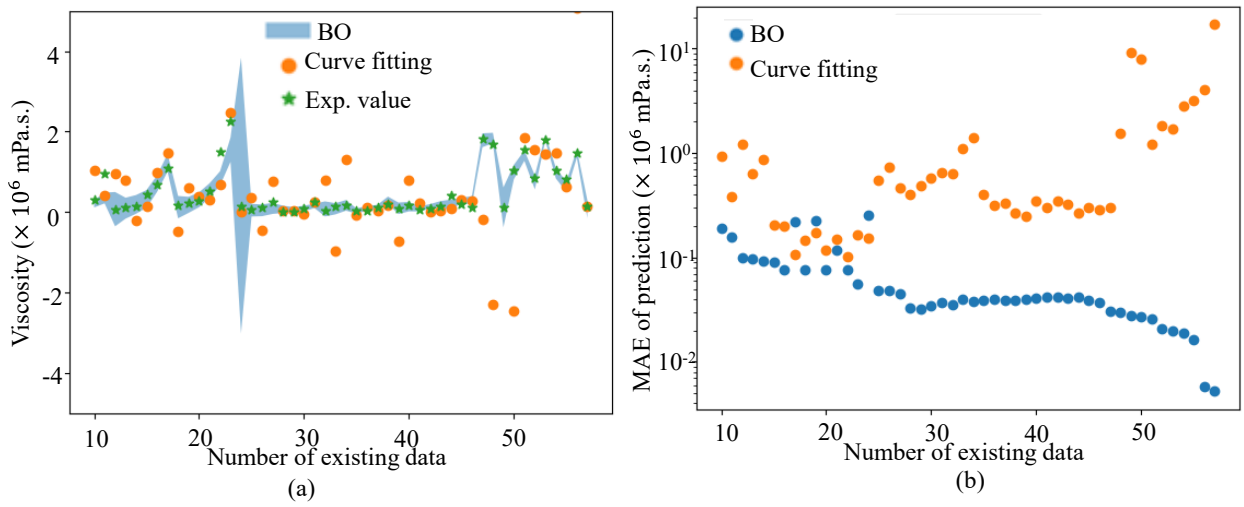

Figure 6. (a) Comparison of how well the BO and curve fitting were predicting the actual experimental viscosity data, and (b) MAE of BO and curve fitting prediction with respect to the number of available experimental data.

We start with 47 initial data points presented in Supplementary Information to train our model. This model suggested the next composition having various weight percent of A, C, and T to improve the prediction of viscosity. Once we determined the viscosity of the suggested composition, the data set was updated including the latest viscosity and the model was run again to get the next composition. We continued our tests ten times to determine the experimental and modeled viscosity data. Experimental data confirmed that our model was closely predicting the viscosity for next composition as shown in Table 1.

Table 1: Comparison between measured and predicted viscosity to validate our proposed framework.

Iteration	Composition	Predicted viscosity ($\times 10^3$), Pa.s.	Measured viscosity ($\times 10^3$), Pa.s.	% error
1	$A_{3.6}C_6T_{0.4}$	1.760	1.830±0.065	4.0
2	$A_4C_{5.4}T_{0.6}$	1.815	1.700±0.03	6.3
3	$A_{0.4}C_{0.6}T_1$	0.118	0.106±0.047	10.1
4	$A_{2.5}C_6T_1$	0.966	1.040±0.03	7.6
5	$A_{3.6}C_{5.4}T_1$	1.361	1.540±0.042	13.15
6	$A_{3.8}C_{5.7}T_{0.4}$	1.819	1.790±0.035	1.6
7	$A_4C_{4.4}T_1$	0.948	1.040±0.123	9.7
8	$A_{2.9}C_{4.7}T_1$	0.736	0.812±0.037	10.32

9	$A_{3.2}C_6T_{0.8}$	1.447	1.480±0.133	2.2
10	$A_{1.3}C_{0.3}T_1$	0.142	0.136±0.004	4.2

A set of four bioink precursors, $A_{0.4}C_{0.6}T_1$, $A_{3.5}C_2T_{0.4}$, $A_{3.5}C_{3.5}T_1$, and $A_{3.8}C_{5.7}T_{0.4}$ are randomly selected for the validation of the surrogate model. The predicted viscosities of $A_{0.4}C_{0.6}T_1$, $A_{3.5}C_2T_{0.4}$, $A_{3.5}C_{3.5}T_1$, and $A_{3.8}C_{5.7}T_{0.4}$ at a shear rate of 1 s^{-1} (preprocessing stage) are 118, 132, 433, and 1818 Pa.s, respectively, and they cover a wide range of viscosities, e.g., [118-1818 Pa.s]. To correlate this information with the processing or deposition stage of bioprinting, a 38 mm diameter bi-layer construct with a 2 mm×2 mm raster width was fabricated as shown in Figure 7. During the deposition stage, the material undergoes deformation, and the degree of transformation depends upon process parameters such as nozzle diameter, applied pressure, print speed, and print distance. Four different sets of process parameters (presented in Supplemental Table 3) are used to print the construct, and their printability is measured using the technique described in our earlier work [55]. Although the printability index increases with an increase in predicted resting viscosity, the process parameter significantly contribute to the printability of the construct. For example, lower resting viscosity requires lower extrusion pressure and can be printed at a faster speed. With an increase in viscosity, the extrusion pressure increases significantly. For medium resting viscosity, the print speed can still remain fast, producing the construct with reasonable printability. For high resting viscosity, we observed high extrusion pressure and much slower speed, which may not be conducive to cell survivability. Therefore, the surrogate model resulting from our BO framework can be used in a meaningful way to achieve a well-defined architecture, reducing the experimental burden and subsequent required resources.

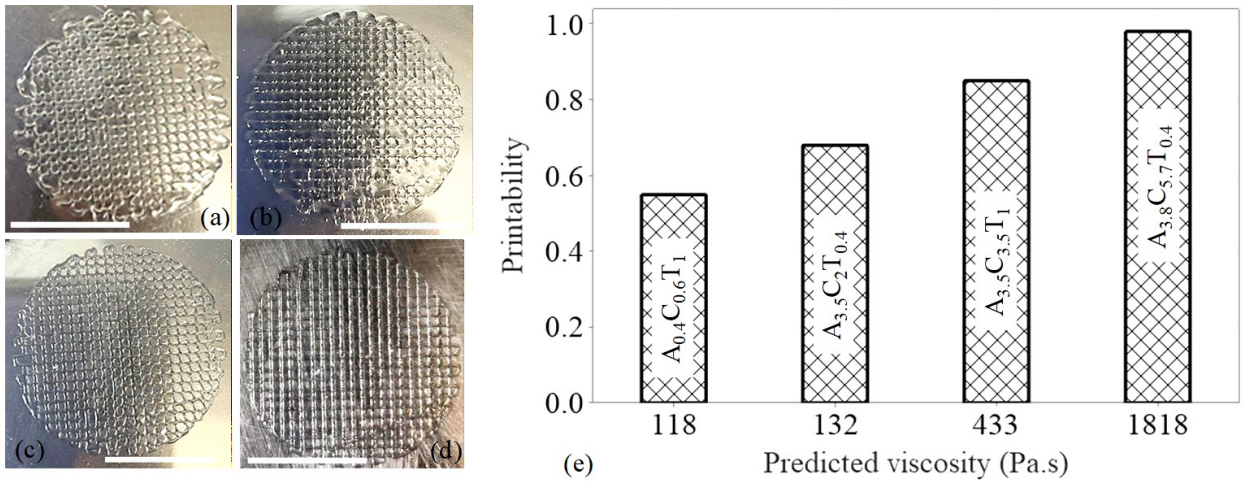

Figure 7: Bi-layer construct fabrication using compositions (a) $A_{0.4}C_{0.6}T_1$, (b) $A_{3.5}C_2T_{0.4}$, (c) $A_{3.5}C_{3.5}T_1$, and (d) $A_{3.8}C_{5.7}T_{0.4}$, (e) the calculate value of printability with respect to the predicted viscosity of those compositions (2 cm scale bar).

4 Conclusion

We utilize a machine learning framework to predict the viscosity of heterogeneous bioink precursor compositions, aiming to enhance extrusion-based bioprinting techniques. Our approach incorporates Bayesian Optimization (BO), leveraging a limited dataset to inform our model, a method especially useful given the sparse data typically available in the bioprinting domain. Informed by domain expertise, a mask function is constructed to define the feasible parameter space suitable for the extrinsic characteristics (e.g., cell viability) for the bioink components and their interactions. The framework is able to differentiate the contribution of individual components of the heterogeneous ink material by predicting the viscosity of the same solid content with different compositions. The outcome from the surrogate model is used to predict the viscosity of random compositions, which are tested for printability. The results show good agreement with the empirical knowledge in the field. With added physics-based model of particulate rheology, the proposed framework can be adopted for bioink (cell-laden biomaterial) materials.

The proposed BO-based machine learning framework presents a highly promising route for advancing the scalability of 3D bioprinting. This is achieved by enhancing the bioink composition selection process through the utilization of intrinsic properties acquired by small-scale experimentation. These bioink property data are fine-tuned to such an extent that the requirement

for repetitive trial and error testing is significantly diminished. Additionally, by tying the intrinsic factor with extrinsic property (e.g., cell viability) of the post processing stage through the mask function, a more managable and functional parameter space is investigated. As a result, our approach holds the potential to streamline and expedite the 3D bioprinting process, making it more efficient and reliable. Nevertheless, its potential for optimizing bioink composition for both mechanical and biological functionality has not been fully validated, primarily due to the complex relationship between the three stages of the bioprinting process. The current compartmentalization of these stages generates constraints from the limited and incomplete dataset for the optimization problem. To address these challenges in future endeavors, we intend to bolster our efforts by generating a more extensive dataset of intrinsic material properties (i.e., modulus, degradation rate, degree of gelation etc.) tied them with multiple extrinsic factors (i.e., shape fidelity, printability, cell proliferation, and differentiation). Such future framework will require adapting the machine learning models with physics-based data augmentation and incorporating additional experimental data for these properties at various stages. The surrogate model for viscosity prediction generated in this research considered the viscosity data at a constant shear rate of 1 s^{-1}. The material undergoes transformation during the deposition stage, and the viscosity at deposition can be significantly different. Additionally, performing this study with bioink (cell-laden biomaterial) can provide more insight into bioprinting living material, which is the limitation of this work and can be considered as future research.

ACKNOWLEDGEMENT

This work was supported by NSF-EPSCoR-BioMade #1757371, NIH-INBRE-IDeA P20GM103506, and FY22 UMaine-Northeastern Seed Grant.

Reference

1. Ouyang, L., C.B. Highley, C.B. Rodell, W. Sun, and J.A. Burdick, *3D printing of shear-thinning hyaluronic acid hydrogels with secondary cross-linking.* ACS Biomaterials Science & Engineering, 2016. **2**(10): p. 1743-1751.
2. Malda, J., J. Visser, F.P. Melchels, T. Jüngst, W.E. Hennink, W.J. Dhert, J. Groll, and D.W. Hutmacher, *25th anniversary article: engineering hydrogels for biofabrication.* Advanced materials, 2013. **25**(36): p. 5011-5028.
3. Kong, H.-J., K.Y. Lee, and D.J. Mooney, *Decoupling the dependence of rheological/mechanical properties of hydrogels from solids concentration.* Polymer, 2002. **43**(23): p. 6239-6246.

4. Dababneh, A.B. and I.T. Ozbolat, *Bioprinting technology: a current state-of-the-art review.* Journal of Manufacturing Science and Engineering, 2014. **136**(6).
5. Maresca, J.A., D.C. DeMel, G.A. Wagner, C. Haase, and J.P. Geibel, *Three-dimensional bioprinting applications for bone tissue engineering.* Cells, 2023. **12**(9): p. 1230.
6. Sun, W., B. Starly, A.C. Daly, J.A. Burdick, J. Groll, G. Skeldon, W. Shu, Y. Sakai, M. Shinohara, and M. Nishikawa, *The bioprinting roadmap.* Biofabrication, 2020. **12**(2): p. 022002.
7. Ng, W.L., J.M. Lee, M. Zhou, Y.-W. Chen, K.-X.A. Lee, W.Y. Yeong, and Y.-F. Shen, *Vat polymerization-based bioprinting—process, materials, applications and regulatory challenges.* Biofabrication, 2020. **12**(2): p. 022001.
8. Chung, J.H., S. Naficy, Z. Yue, R. Kapsa, A. Quigley, S.E. Moulton, and G.G. Wallace, *Bio-ink properties and printability for extrusion printing living cells.* Biomaterials Science, 2013. **1**(7): p. 763-773.
9. Jessop, Z.M., A. Al-Sabah, N. Gao, S. Kyle, B. Thomas, N. Badiei, K. Hawkins, and I.S. Whitaker, *Printability of pulp derived crystal, fibril and blend nanocellulose-alginate bioinks for extrusion 3D bioprinting.* Biofabrication, 2019. **11**(4): p. 045006.
10. Xu, T., J. Jin, C. Gregory, J.J. Hickman, and T. Boland, *Inkjet printing of viable mammalian cells.* Biomaterials, 2005. **26**(1): p. 93-99.
11. Wu, D. and C. Xu, *Predictive modeling of droplet formation processes in inkjet-based bioprinting.* Journal of Manufacturing Science and Engineering, 2018. **140**(10).
12. Mukhangaliyeva, A., D. Dairabayeva, A. Perveen, and D. Talamona, *Optimization of Dimensional Accuracy and Surface Roughness of SLA Patterns and SLA-Based IC Components.* Polymers, 2023. **15**(20): p. 4038.
13. Groll, J., J. Burdick, D. Cho, B. Derby, M. Gelinsky, S. Heilshorn, T. Jüngst, J. Malda, V. Mironov, and K. Nakayama, *A definition of bioinks and their distinction from biomaterial inks.* Biofabrication, 2018. **11**(1): p. 013001.
14. Dell, A.C., G. Wagner, J. Own, and J.P. Geibel, *3D bioprinting using hydrogels: cell inks and tissue engineering applications.* Pharmaceutics, 2022. **14**(12): p. 2596.
15. Habib, M.A. and B. Khoda. *A Rheological Study of Bio-Ink: Shear Stress and Cell Viability*. in *International Manufacturing Science and Engineering Conference*. 2021. American Society of Mechanical Engineers.
16. Gudapati, H., M. Dey, and I. Ozbolat, *A comprehensive review on droplet-based bioprinting: Past, present and future.* Biomaterials, 2016. **102**: p. 20-42.
17. Chahal, D., A. Ahmadi, and K.C. Cheung, *Improving piezoelectric cell printing accuracy and reliability through neutral buoyancy of suspensions.* Biotechnology and bioengineering, 2012. **109**(11): p. 2932-2940.
18. Dou, C., V. Perez, J. Qu, A. Tsin, B. Xu, and J. Li, *A state-of-the-art review of laser-assisted bioprinting and its future research trends.* ChemBioEng Reviews, 2021. **8**(5): p. 517-534.
19. Chang, J. and X. Sun, *Laser-induced forward transfer based laser bioprinting in biomedical applications.* Frontiers in Bioengineering and Biotechnology, 2023. **11**.
20. Morgan, F.L.C., L. Moroni, and M.B. Baker, *Dynamic Bioinks to Advance Bioprinting.* Advanced Healthcare Materials, 2020. **9**(15): p. 1901798.
21. Moroni, L., T. Boland, J.A. Burdick, C. De Maria, B. Derby, G. Forgacs, J. Groll, Q. Li, J. Malda, and V.A. Mironov, *Biofabrication: a guide to technology and terminology.* Trends in biotechnology, 2018. **36**(4): p. 384-402.
22. Schwab, A., R. Levato, M. D'Este, S. Piluso, D. Eglin, and J. Malda, *Printability and shape fidelity of bioinks in 3D bioprinting.* Chemical reviews, 2020. **120**(19): p. 11028-11055.

23. Di Giuseppe, M., N. Law, B. Webb, R.A. Macrae, L.J. Liew, T.B. Sercombe, R.J. Dilley, and B.J. Doyle, *Mechanical behaviour of alginate-gelatin hydrogels for 3D bioprinting.* Journal of the mechanical behavior of biomedical materials, 2018. **79**: p. 150-157.
24. Agarwal, T., S.G.H. Narayana, K. Pal, K. Pramanik, S. Giri, and I. Banerjee, *Calcium alginate-carboxymethyl cellulose beads for colon-targeted drug delivery.* International journal of biological macromolecules, 2015. **75**: p. 409-417.
25. Gonzalez-Fernandez, T., A.J. Tenorio, K.T. Campbell, E.A. Silva, and J.K. Leach, *Alginate-based bioinks for 3D bioprinting and fabrication of anatomically accurate bone grafts.* Tissue Engineering Part A, 2021.
26. Narayanan, L.K., P. Huebner, M.B. Fisher, J.T. Spang, B. Starly, and R.A. Shirwaiker, *3D-bioprinting of polylactic acid (PLA) nanofiber–alginate hydrogel bioink containing human adipose-derived stem cells.* ACS Biomaterials Science & Engineering, 2016. **2**(10): p. 1732-1742.
27. Nguyen, D., D.A. Hägg, A. Forsman, J. Ekholm, P. Nimkingratana, C. Brantsing, T. Kalogeropoulos, S. Zaunz, S. Concaro, and M. Brittberg, *Cartilage tissue engineering by the 3D bioprinting of iPS cells in a nanocellulose/alginate bioink.* Scientific reports, 2017. **7**(1): p. 658.
28. Li, V.C., A. Mulyadi, C.K. Dunn, Y. Deng, and H.J. Qi, *Direct Ink Write 3D Printed Cellulose Nanofiber Aerogel Structures with Highly Deformable, Shape Recoverable, and Functionalizable Properties.* ACS Sustainable Chemistry & Engineering, 2018. **6**(2): p. 2011-2022.
29. Habib, A. and B. Khoda, *Development of clay based novel hybrid bio-ink for 3D bio-printing process.* Journal of Manufacturing Processes, 2019. **38**: p. 76-87.
30. Colosi, C., S.R. Shin, V. Manoharan, S. Massa, M. Costantini, A. Barbetta, M.R. Dokmeci, M. Dentini, and A. Khademhosseini, *Microfluidic Bioprinting of Heterogeneous 3D Tissue Constructs Using Low-Viscosity Bioink.* Advanced Materials, 2016. **28**(4): p. 677-684.
31. Rastin, H., R.T. Ormsby, G.J. Atkins, and D. Losic, *3D Bioprinting of Methylcellulose/Gelatin-Methacryloyl (MC/GelMA) Bioink with High Shape Integrity.* ACS Applied Bio Materials, 2020. **3**(3): p. 1815-1826.
32. Ahlfeld, T., G. Cidonio, D. Kilian, S. Duin, A. Akkineni, J. Dawson, S. Yang, A. Lode, R. Oreffo, and M. Gelinsky, *Development of a clay based bioink for 3D cell printing for skeletal application.* Biofabrication, 2017. **9**(3): p. 034103.
33. Cooke, M.E. and D.H. Rosenzweig, *The rheology of direct and suspended extrusion bioprinting.* APL bioengineering, 2021. **5**(1): p. 011502.
34. Habib, A., R. Sarah, S. Tuladhar, B. Khoda, and S.M. Limon, *Modulating rheological characteristics of bio-ink with component weight and shear rate for enhanced bioprinted scaffold fidelity.* Bioprinting, 2024. **38**: p. e00332.
35. Zhou, P., C. Yuan, and X. Yan, *Computational approaches for understanding and predicting the self-assembled peptide hydrogels.* Current Opinion in Colloid & Interface Science, 2022: p. 101645.
36. Pasquino, R., N. Grizzuti, P.L. Maffettone, and F. Greco, *Rheology of dilute and semidilute noncolloidal hard sphere suspensions.* Journal of Rheology, 2008. **52**(6): p. 1369-1384.
37. Luukkonen, P., T. Schæfer, L. Hellén, A.M. Juppo, and J. Yliruusi, *Rheological characterization of microcrystalline cellulose and silicified microcrystalline cellulose wet masses using a mixer torque rheometer.* International journal of pharmaceutics, 1999. **188**(2): p. 181-192.
38. Shao, Y., D. Chaussy, P. Grosseau, and D. Beneventi, *Use of microfibrillated cellulose/lignosulfonate blends as carbon precursors: Impact of hydrogel rheology on 3D printing.* Industrial & Engineering Chemistry Research, 2015. **54**(43): p. 10575-10582.
39. Kiyotake, E.A., A.W. Douglas, E.E. Thomas, S.L. Nimmo, and M.S. Detamore, *Development and quantitative characterization of the precursor rheology of hyaluronic acid hydrogels for bioprinting.* Acta biomaterialia, 2019. **95**(Sep 1): p. 176-187.

40. Erps, T., M. Foshey, M.K. Luković, W. Shou, H.H. Goetzke, H. Dietsch, K. Stoll, B. von Vacano, and W. Matusik, *Accelerated discovery of 3D printing materials using data-driven multiobjective optimization.* Science Advances, 2021. **7**(42): p. eabf7435.
41. Lee, J., S.J. Oh, S.H. An, W.-D. Kim, and S.-H. Kim, *Machine learning-based design strategy for 3D printable bioink: Elastic modulus and yield stress determine printability.* Biofabrication, 2020. **12**(3): p. 035018.
42. Malekpour, A. and X. Chen, *Printability and cell viability in extrusion-based bioprinting from experimental, computational, and machine learning views.* Journal of Functional Biomaterials, 2022. **13**(2): p. 40.
43. An, J., C.K. Chua, and V. Mironov, *Application of machine learning in 3D bioprinting: focus on development of big data and digital twin.* International journal of bioprinting, 2021. **7**(1).
44. Li, H., H. Tian, Y. Chen, S. Xiao, X. Zhao, Y. Gao, and L. Zhang, *Analyzing and Predicting the Viscosity of Polymer Nanocomposites in the Conditions of Temperature, Shear Rate, and Nanoparticle Loading with Molecular Dynamics Simulations and Machine Learning.* The Journal of Physical Chemistry B, 2023. **127**(15): p. 3596-3605.
45. Bone, J.M., C.M. Childs, A. Menon, B. Poczos, A.W. Feinberg, P.R. LeDuc, and N.R. Washburn, *Hierarchical machine learning for high-fidelity 3D printed biopolymers.* ACS Biomaterials Science & Engineering, 2020. **6**(12): p. 7021-7031.
46. Webb, B. and B.J. Doyle, *Parameter optimization for 3D bioprinting of hydrogels.* Bioprinting, 2017. **8**: p. 8-12.
47. Ruberu, K., M. Senadeera, S. Rana, S. Gupta, J. Chung, Z. Yue, S. Venkatesh, and G. Wallace, *Coupling machine learning with 3D bioprinting to fast track optimisation of extrusion printing.* Applied Materials Today, 2021. **22**: p. 100914.
48. Freeman, S., S. Calabro, R. Williams, S. Jin, and K. Ye, *Bioink formulation and machine learning-empowered bioprinting optimization.* Frontiers in Bioengineering and Biotechnology, 2022. **10**: p. 913579.
49. Ma, W., F. Cheng, Y. Xu, Q. Wen, and Y. Liu, *Probabilistic Representation and Inverse Design of Metamaterials Based on a Deep Generative Model with Semi-Supervised Learning Strategy.* Adv Mater, 2019. **31**(35): p. e1901111.
50. Guo, J.L., M. Januszyk, and M.T. Longaker, *Machine learning in tissue engineering.* Tissue Engineering Part A, 2023. **29**(1-2): p. 2-19.
51. Freedman, D.A., *Statistical models: theory and practice*. 2009: cambridge university press.
52. Cortes, C. and V. Vapnik, *Support-vector networks.* Machine learning, 1995. **20**: p. 273-297.
53. Fix, E. and J.L. Hodges, *Discriminatory analysis. Nonparametric discrimination: Consistency properties.* International Statistical Review/Revue Internationale de Statistique, 1989. **57**(3): p. 238-247.
54. Habib, M. and B. Khoda, *Fiber Filled Hybrid Hydrogel for Bio-Manufacturing.* Journal of Manufacturing Science and Engineering, 2021. **143**(4): p. 041013.
55. Habib, A., V. Sathish, S. Mallik, and B. Khoda, *3D Printability of Alginate-Carboxymethyl Cellulose Hydrogel.* Materials, 2018. **11**(3): p. 454.
56. Xue, D., P.V. Balachandran, J. Hogden, J. Theiler, D. Xue, and T. Lookman, *Accelerated search for materials with targeted properties by adaptive design.* Nature communications, 2016. **7**(1): p. 1-9.
57. Xue, D., P.V. Balachandran, R. Yuan, T. Hu, X. Qian, E.R. Dougherty, and T. Lookman, *Accelerated search for BaTiO3-based piezoelectrics with vertical morphotropic phase boundary using Bayesian learning.* Proceedings of the National Academy of Sciences, 2016. **113**(47): p. 13301-13306.

58. Jodat, Y.A., K. Kiaee, D. Vela Jarquin, R.L. De la Garza Hernández, T. Wang, S. Joshi, Z. Rezaei, B.A.G. de Melo, D. Ge, and M.S. Mannoor, *A 3D-printed hybrid nasal cartilage with functional electronic olfaction.* Advanced Science, 2020. **7**(5): p. 1901878.
59. Xiong, R., Z. Zhang, W. Chai, Y. Huang, and D.B. Chrisey, *Freeform drop-on-demand laser printing of 3D alginate and cellular constructs.* Biofabrication, 2015. **7**(4): p. 045011.
60. Majumder, N., A. Mishra, and S. Ghosh, *Effect of varying cell densities on the rheological properties of the bioink.* Bioprinting, 2022. **28**: p. e00241.
61. Einstein, A., *Eine neue Bestimmung der Moleküldimensionen.* 1906. **324**(2): p. 289-306.

Supplementary Information

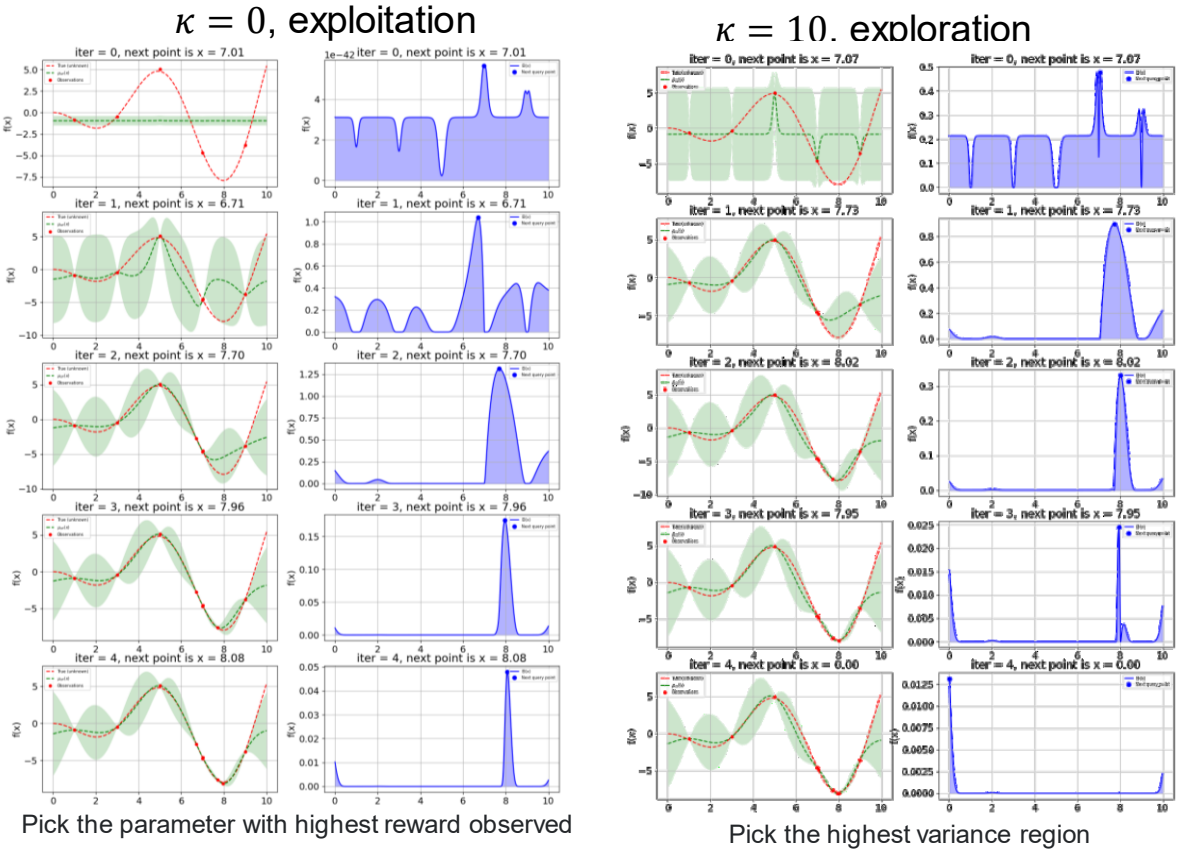

Figure S1. Effect of κ at a various value.

Table S1: Initial dataset comprises material composition and corresponding viscosity data.

A (%)	C (%)	T(%)	Viscosity (Pa.s.)	A (%)	C (%)	T(%)	Viscosity (Pa.s.)
4	6	0	2256	1	3	1	131
4	5	0	1511	2	3	0.5	131
3	6	0	1103	4	2	0.5	124
2	6	0	965	3	2	0	110
3	5	0	676	1	5	0	104
4	4	0	534	3	2	0.5	94
3	4	0	434	1	3	0.5	94
4	1	1	424	3	1	1	91
1	6	0	410	3	1	0.5	71
2	5	0	313	1	4	0	69
4	3	0	280	3	1	0	68
2	4	0	275	2	3	0	64
1	4	1	248	1	2	1	58
1	4	0.5	247	1	3	0	55
4	2	0	229	2	2	0	55
2	4	0.5	204	2	2	0.5	45
4	1	0.5	194	2	1	1	36
3	2	1	184	2	1	0.5	31
4	1	0	167	1	2	0	28
2	3	1	167	2	1	0	16
3	3	0.5	156	1	2	0.5	11.5
3	3	0	149	1	1	0.5	2.5
2	2	1	148	1	1	0	2.3
1	1	1	144				

Table S2: Initial dataset comprises material composition and corresponding cell viability data.

A (%)	C (%)	T (%)	Cell viability (%)
4	4	0	86
4	3	0	84
4	2	0	83
4	1	0	81
2	2	1	91
1	1	1	88
1	3	1	92
3	2	0	87
3	1	1	89
1	4	0	89
2	3	0	88
2	2	0.5	90

Table S3: Predicted viscosity and measure printability.

Compositions	Predicted Viscosity (Pa.s)	Process parameters			Image	printability
		Nozzle dia (µm)	Pressure (psi)	Print speed (mm/s)		
$A_{0.4}C_{0.6}T_1$	118	310	5	8.33		0.55
$A_{3.5}C_2T_{0.4}$	132	310	12	12	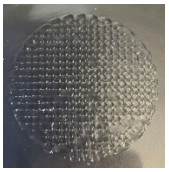	0.68
$A_{3.5}C_{3.5}T_1$	433	310	30	12	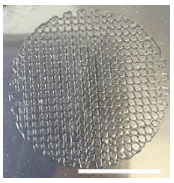	0.85
$A_{3.8}C_{5.7}T_{0.4}$	1818	310	40	0.83	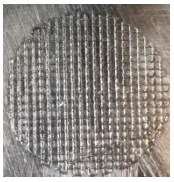	0.98